A Mixed Flux Coupler and Dual-Path Parallel Compensation Based Rotating Wireless Power Transfer System Integrated With Rotational Speed Monitoring Function

Longyang Wang, Jiangui Li, Guangbin Luo, Qinghe Si, Zheyuan Guo, Yinchong Peng, and Ian Robertson, *Fellow, IEEE*

***Abstract*—A rotating wireless power transfer system based on a mixed flux coupler and dual-path parallel compensation is proposed in this article. It can achieve stable and efficient wireless power transmission as well as accurate speed monitoring without adding an additional excitation, solving the problems of voltage instability and low efficiency in existing solutions. First, the system topology and working principle are presented. Then, the working characteristics of the mixed flux coupler are analyzed and optimized. The power, efficiency, and voltage gain formulas are derived for the system based on a dual-coupled inductor–capacitor–capacitor-series compensation. Based on these theories and the functions that need to be achieved, a number of key design criteria are discussed. Practical experiments on rotating wireless power transmission, speed measurement, and dual-load interference have been carried out. The experimental results show that the proposed system can achieve accurate speed monitoring and stable wireless power transmission. The maximum power of the system can reach 163.59 W, and a maximum efficiency of more than 80% can be achieved. The proposed technique has the potential to significantly contribute to the further development of wireless power transfer technology for rotating machines, such as wind turbines, machining equipment, and robot joints.**

***Index Terms*—Dual-path parallel compensation, magnetic flux, mixed flux coupler, rotating machines, speed measurement, wireless power transfer (WPT).**

I. INTRODUCTION

WITH the rapid advancement of technology, a large number of rotating devices serve a wide range of applications, even in harsh working environments such as wind turbines [1], and high-precision machining equipment [2], [3], [4], [5]. Power transfer from a stationary structure to a rotating part is a common requirement for many rotating devices. For instance, in wind turbines, to avoid faults, such as fatigue cracks and wear in blades, active thermography instruments and stress monitors are typically installed to monitor their structural condition in real-time under long-term, multidimensional loading and harsh natural conditions. To supply power to the monitoring and communication equipment, a power transfer system capable of operating in extreme temperature and humidity environments is essential [1]. In high-precision machine tools, ultrasonic equipment is usually employed to improve machining accuracy. The ultrasonic device is installed on the rotating main spindle of the machine tool, and it requires a power transfer system capable of operating in dusty and high-vibration environments [2], [3], [4], [5]. Similar scenarios can also be found in fields with harsh working environments, such as "pipebots" [6], which aim to develop robots that can autonomously inspect buried sewer and freshwater pipe networks, as well as in aerospace and smart manufacturing.

The traditional approaches to transfer power to rotating devices are to use conducting slip rings with brushes, or rotary transformers [7], [8], [9]. Slip rings and brushes are a commonly used, cost-effective means of providing contact-based rotating power transfer. However, they may have issues with a short lifespan and poor safety and are not suitable for use in harsh environments. Rotary transformers are a simple form of contactless rotating power transmission system. They have stable performance and strong anti-interference ability, but their design is inflexible, and the efficiency is low at low power.

In addition to these two techniques, magnetic-coupled resonant rotating wireless power transfer (MCR-R-WPT) technology has received widespread attention from scholars in recent years [10], [11], [12], [13]. MCR-R-WPT technology, such as rotary transformers, uses copper coils to generate a magnetic field for power transfer, which means both of them have similar interference resistance and environmental adaptability. However, the difference lies in the fact that, compared to rotary transformers, MCR-R-WPT technology operates at a higher frequency range (20 kHz to 5 MHz), enabling it to achieve

---

Manuscript received 30 November 2023; revised 21 January 2024; accepted 24 February 2024. Date of publication 5 March 2024; date of current version 19 April 2024. This work was supported in part by the China Scholarship Council under Projects CXXM20210159, and in part by the Engineering and Physical Science Research Council (UK) under Grant EP/S016813/1, Pervasive Sensing for Buried Pipes (Pipebots: Theme 6, Communications and Power). Recommended for publication by Associate Editor J. Acero. *(Corresponding author: Jiangui Li.)*

Longyang Wang, Jiangui Li, Guangbin Luo, Qinghe Si, Zheyuan Guo, and Yinchong Peng are with the School of Mechanical and Electronic Engineering, Wuhan University of Technology, Wuhan 430070, China (e-mail: wanglongyang@whut.edu.cn; jianguili@whut.edu.cn; guangbinluo@whut.edu.cn; qinghesi@whut.edu.cn; guozheyuan@whut.edu.cn; ycp1928563519@whut.edu.cn).

Ian Robertson is with the School of Electronic and Electrical Engineering, University of Leeds, LS2 9JT Leeds, U.K. (e-mail: i.d.robertson@leeds.ac.uk).

Color versions of one or more figures in this article are available at https://doi.org/10.1109/TPEL.2024.3373651.

Digital Object Identifier 10.1109/TPEL.2024.3373651

longer transmission distances (1 cm or more) and higher efficiency. This means that MCR-R-WPT technology offers greater design flexibility. Wang et al. [10] proposed a redundant and fault-tolerant design method for the MCR-R-WPT system and put forward active and passive fault-tolerant control methods for the WPT system. The system can quickly diagnose and eliminate faults in the WPT system by implementing monitoring of electromagnetic parameters. The design of an MCR-R-WPT system with stable power and efficiency to prevent rotation displacement for underwater drones was presented in [11]. The coil structure of the system consists of two decoupled receivers, each of which is composed of two reverse-wound coils. Under optimal conditions, the transmission efficiency of the system was shown to reach 92.26%, and the transmission power could reach 664 W. A compact, rotation-free, and high-power density MCR-R-WPT system for robot joints was presented in [12]. MCR-R-WPT has also been employed in the design of a highly efficient, safe, and stable system for the solar wings of a spacecraft [13]. In conclusion, for powering rotating equipment in harsh working environments, MCR-R-WPT technology is a better choice compared to brushes and slip rings, and rotary transformers, due to its safety, efficiency, environmental adaptability, and flexible design.

In harsh working environments, in addition to rotating power transfer, measuring the rotational speed of rotating parts is typically required in the development, use, testing, and maintenance procedures to control the movement of the mechanism. For example, in wind turbines, apart from providing power to sensors on the blades through rotating power transfer for blade condition monitoring, it is also necessary to monitor the real-time rotational speed of the wind turbine. This rotational speed is a key parameter for determining whether it is operating normally. In high-precision machining, apart from supplying power to ultrasonic devices for auxiliary machining through rotating power transfer, it is also essential to monitor the rotational speed of the machining drill bits in order to enhance overall machining precision.

Currently, commonly used rotational speed measurement devices can generally be divided into mechanical, photoelectric, and electromagnetic types based on their working principle [14]. Each type has its own characteristics: Mechanical speed measurement devices have a simple structure and low cost, but they are prone to affecting the inherent parameters of the object being measured, such as damping and frequency. Photoelectric speed measurement devices are compact in size but perform poorly in extreme temperature, extreme humidity, high dust, and other environments with high pollutant levels. Electromagnetic sensors are the most suitable for use as rotational speed sensors in harsh working environments because they collect speed through the electromagnetic field, which is almost unaffected by environmental conditions and interference. However, their large size is often not conducive to the overall miniaturization of the system.

The previous discussion has highlighted the significance of rotating power transfer and rotational speed monitoring in fields such as wind turbines, robotics, and high-precision machining tools. Furthermore, it is concluded that MCR-R-WPT technology and electromagnetic sensors are the best solutions for achieving rotating power transfer and speed monitoring, respectively, in harsh working environments. However, simultaneously installing these two subsystems in rotating equipment will undoubtedly occupy valuable space on the narrow mounting shaft, as these two subsystems have their independent power sources, controls, and monitoring units. This will undoubtedly increase their complexity of implementation.

To solve this problem and improve the integration of the system, an MCR-R-WPT system based on a radial-flux coupler was proposed in [15]. With a single excitation source, the rotational speed of the shaft can be calculated by monitoring the output voltage changes caused by the coupler's mutual inductance variation. Therefore, this system allows for simultaneous wireless power transfer and speed monitoring. It can be advantageous in improving the integration of rotating equipment to some extent. However, this system also has some drawbacks: output voltage fluctuations result in lower overall efficiency, and it can be detrimental to the normal operation of the load.

This article proposes a wireless power transfer system based on a mixed-flux coupler and dual-path parallel compensation to achieve both wireless power transfer and shaft speed monitoring simultaneously. Compared to the system presented in [15], the proposed system provides a stable output voltage and higher output efficiency, and the wireless power transmission and speed detection do not interfere with each other. The basic operating principles of the proposed system are first introduced from the perspective of the mixed-flux coupler and the dual-path parallel compensation circuit. Then, the rotational and self-decoupling characteristics of the mixed-flux coupler are analyzed, and the coupler is optimized in terms of coupling characteristics and magnetic field distribution. To address the issue of the coupler being easily affected by the metal shaft, a magnetic shielding device has been designed. Then, the dual-path parallel inductor–capacitor–capacitor-series (LCC-S) compensation circuit technique is introduced. Expressions for the output power, efficiency, and dual-path voltage gain of the system are derived. In order to facilitate the controller in capturing the speed signal, a signal processing circuit has been employed. Finally, practical results for an experimental platform using the wireless power transfer system based on the mixed-flux coupler and the dual-path parallel compensation are presented, including wireless power transfer performance, speed measurement, and performance with a variable load.

II. WORKING PRINCIPLE

The proposed MCR-R-WPT system is based on a mixed flux coupler and dual-path parallel compensation, which can achieve rotational wireless power transmission and speed measurement simultaneously. Fig. 1 shows the two types of couplers that make up the mixed flux coupler: namely, a radial flux coupler and an axial flux coupler. Both couplers comprise transmitting and receiving coils. The coils in yellow in Fig. 1 are the transmitting coils of the two couplers, while the coils in blue are their corresponding receiving coils. The transmitting and receiving coils of the radial flux coupler consist of multiple rectangular coils connected end-to-end around the rotation axis, while the axial flux coupler is made up of multiple layers of helical coils.

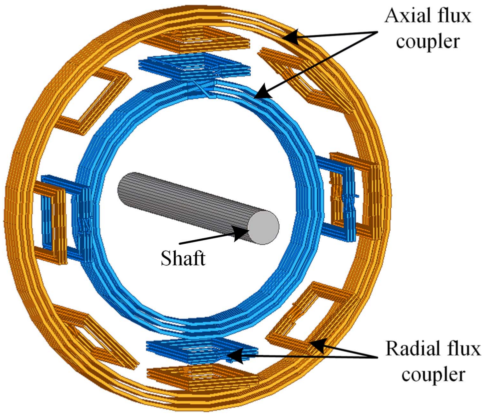

Fig. 1. Mixed flux coupler.

All transmitting coils are stationary, and all receiving coils rotate along with the shaft.

When energized, the radial flux coupler produces a magnetic flux perpendicular to the shaft axis, while the axial flux coupler produces a magnetic flux parallel to the axis. The coupling degree of the radial flux coupler varies periodically with the rotation angle due to its special coil structure, while the coupling degree of the axial flux coupler remains relatively constant. Changes in the coupling degree of the radial flux coupler cause changes in the output voltage of the pathway it is in.

According to the Fourier transform, the high-frequency inverter's square wave voltage output can be represented as a combination of the fundamental frequency and harmonic components [16]. A compensation circuit is used to selectively input the fundamental frequency component into the axial flux coupler and the third harmonic component into the radial flux coupler, as shown in Fig. 2. The path through which the fundamental frequency component of the inverter output voltage flows is called the fundamental path, while the path through which the third harmonic component flows is called the harmonic path. Due to the stable mutual inductance of the axial flux coupler, efficient and stable rotational wireless power transmission can be achieved along the fundamental path. Meanwhile, by monitoring the output voltage of the harmonic path in relation to the rotation angle and coupling degree, the rotational speed can be determined.

III. CHARACTERISTICS OF MIXED FLUX COUPLER

A. Rotating Characteristics

In the mixed flux coupler, the coupling characteristics of the axial flux coupler remain stable as the shaft rotates, while the coupling characteristics of the radial flux coupler change with the rotation. The rotation diagram of the receiver of the radial flux coupler and the variation of the mutual inductance over time are shown in Fig. 3. The coupling degree of the radial flux coupler is maximum when the blue coil is perfectly aligned with the yellow coil (0°), and it reaches the minimum when the blue coil rotates 22.5°. After a further 22.5° rotation, the blue and yellow coils are aligned again, and the coupling degree reaches the maximum again, completing one cycle of rotation. The change cycle is determined by the rotation speed of the rotation axis and the number of rectangular coils at the transmitter and receiver. By monitoring the change cycle of mutual inductance, the rotation angle of the rotation axis can be inferred, and then the rotation speed of the shaft can be determined. In Fig. 3, when the receiver of the radial flux coupler rotates 45°, the mutual inductance completes one cycle.

B. Self-Decoupling

Through reasonable magnetic circuit design, two coils can achieve self-decoupling [17]. The mixed flux coupler proposed in this article has this self-decoupling characteristic; that is, there is no cross-coupling between the radial flux coupler and the axial flux coupler. This feature can avoid interference between the radial flux coupler and the axial flux coupler, thereby ensuring stable rotating wireless power transmission and speed monitoring at the same time.

The following is the demonstration of the self-decoupling of the radial and axial flux couplers. The strength of the coupling between the two coils can be determined by the magnitude of the magnetic flux linking the other coil when an electrical current is passed through one of the coils [18], as shown in Fig. 4. $\Psi_{\alpha\alpha}$ represents the self-induced magnetic flux generated by the current i_α passing through coil α, part of which passes through coil β and is represented by $\Psi_{\alpha\beta}$. $\Psi_{\beta\beta}$ represents the self-induced magnetic flux generated by the current i_β passing through coil β, part of which passes through coil α and is represented by $\Psi_{\beta\alpha}$.$\Psi_{\alpha\alpha}$, $\Psi_{\beta\beta}$, $\Psi_{\alpha\beta}$, and $\Psi_{\beta\alpha}$ can be obtained from

$$\begin{cases} \Psi_{\alpha\alpha} = N_\alpha \varphi_{\alpha\alpha} = L_\alpha i_\alpha \\ \Psi_{\beta\beta} = N_\beta \varphi_{\beta\beta} = L_\beta i_\beta \\ \Psi_{\alpha\beta} = N_\beta \varphi_{\alpha\beta} = M_{\alpha\beta} i_\alpha \\ \Psi_{\beta\alpha} = N_\alpha \varphi_{\beta\alpha} = M_{\beta\alpha} i_\beta \end{cases} \tag{1}$$

where N_α and N_β represent the number of turns in coil α and coil β, respectively; $\varphi_{\alpha\alpha}$ and $\varphi_{\beta\beta}$ represent the self-inductance flux of coil α and coil β, respectively; $\varphi_{\alpha\beta}$ represent the flux produced by coil α that passes through coil β, and $\varphi_{\beta\alpha}$ represent the flux produced by coil β that passes through coil α; L_α and L_β represent the self-inductance coefficients of coil α and coil β, respectively; and $M_{\alpha\beta}$ and $M_{\beta\alpha}$ represent the mutual inductances of coil α and coil β, and being of equal magnitude.

According to (1), it can be observed that the strength of the coupling degree of the coupler increases as $\varphi_{\alpha\beta}$ and $\varphi_{\beta\alpha}$ become larger, and vice versa. The values of $\varphi_{\alpha\beta}$ and $\varphi_{\beta\alpha}$ can be obtained from

$$\begin{cases} \varphi_{\alpha\beta} = B_{\alpha\beta} S_{\alpha\beta} \\ \varphi_{\beta\alpha} = B_{\beta\alpha} S_{\beta\alpha} \end{cases} \tag{2}$$

where $B_{\alpha\beta}$ and $B_{\beta\alpha}$ represent the effective magnetic fields produced by coil α and coil β, respectively, while $S_{\alpha\beta}$ and $S_{\beta\alpha}$ represent the effective magnetic flux areas. Combining (1) and (2), it can be concluded that decoupling between the two coils can be achieved when $S_{\alpha\beta} = S_{\beta\alpha} = 0$.

The magnetic flux generated by a single-turn radial coil and an axial coil is illustrated in Fig. 5. The magnetic flux generated

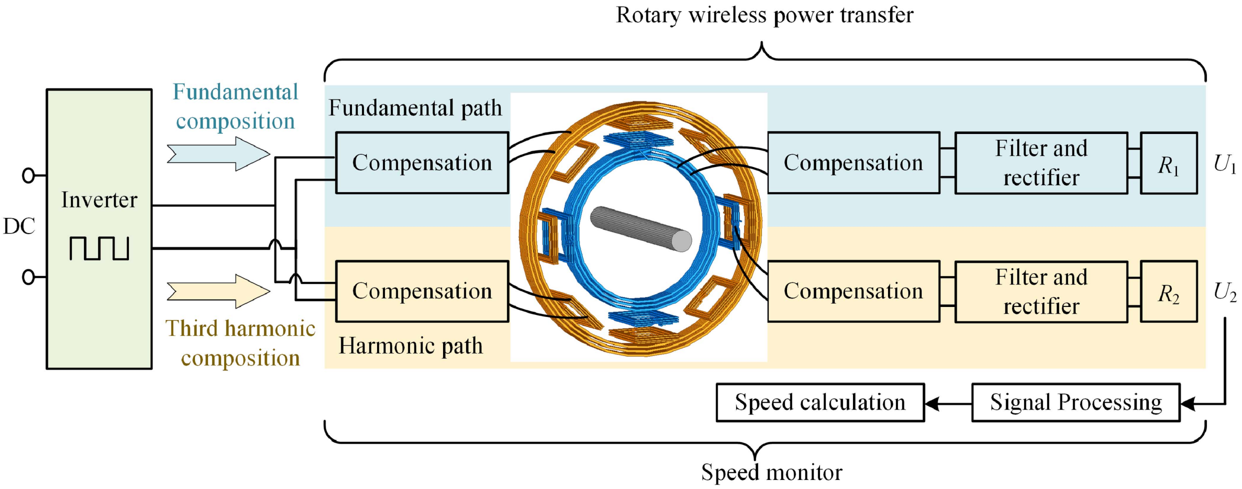

Fig. 2. Mixed flux coupler based MCR-R-WPT system.

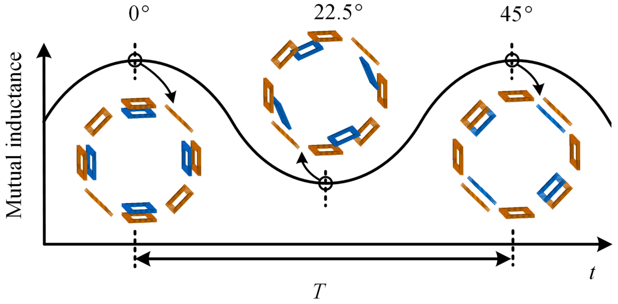

Fig. 3. Mutual inductance variation of radial flux coupler.

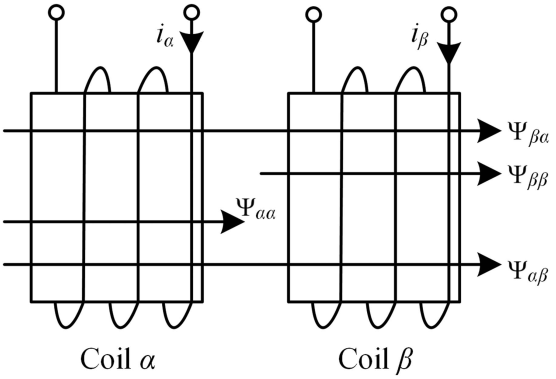

Fig. 4. Coils coupling diagram.

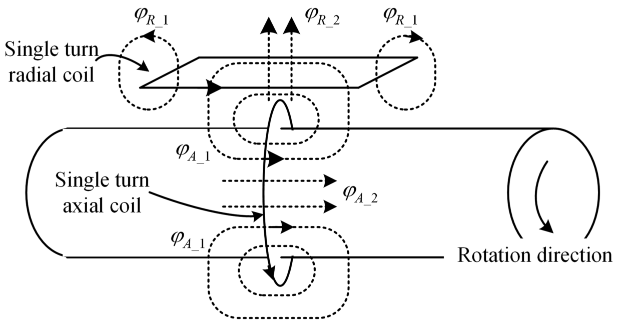

Fig. 5. Magnetic flux generated by single-turn radial coil and axial coil.

TABLE I
COUPLING BETWEEN A SINGLE-TURN RADIAL COIL AND A SINGLE-TURN AXIAL COIL

Content	Value
Self-inductance of radial coil	0.24 μH
Self-inductance of axial coil	0.07 μH
Mutual inductance	1.79e-4 μH
Coupling coefficient	1.4e-3

by the axial coil is composed of φ_{A_1} and φ_{A_2}, where φ_{A_1} is the self-coupling flux of the coil and φ_{A_2} is the component of the flux generated by the coil that passes through the other axial coil. The flux generated by the radial coil consists of φ_{R_1} and φ_{R_2}, where φ_{R_1} is the self-coupling flux of the coil and φ_{R_2} is the component of the flux generated by the coil that passes through the other radial coil.

Based on the loop theorem of magnetic fields, the magnetic flux φ_{A_1} generated by the axial coil must pass through the radial coil and return to the axial coil, forming a closed loop [19]. When the axial coil is positioned directly below the radial coil, the effective area of φ_{A_1} passing through the radial coil is equal in both directions, resulting in the magnetic flux generated by the axial coil not passing through the radial coil. In addition, the magnetic flux generated by the radial coil does not pass through the axial coil, indicating that there is no coupling between them.

To verify this point, a finite element simulation experiment was conducted with the coil positions set as shown in Fig. 5. The radial coil has a length of 30 mm and a width of 20 mm, with a distance of 42 mm between its center and the axis, and the axial coil has a diameter of 76 mm. The calculated self-inductance and mutual inductance are given in Table I. Based on the simulation results, the coupling coefficient between the single-turn axial coil and radial coil is only 1.4e-3, which can be ignored. Thus, under ideal circumstances, the radial flux coil and axial flux coil achieve self-decoupling. Consequently, in the subsequent magnetic field and circuit analyses, only the effective coupling of the mixed flux coupler will be considered.

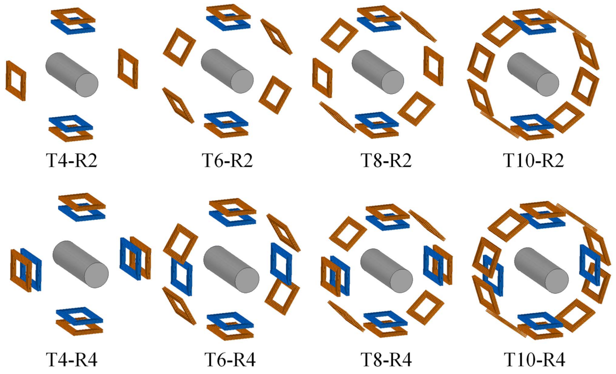

Fig. 6. Radial flux coupler models.

IV. OPTIMIZATION AND ANALYSIS OF MIXED FLUX COUPLER

A. Radial Flux Coupler

In the previous section, it was noted that the cycle of mutual inductance variation in the radial flux coupler depends on the number of rectangular coils at the transmitting and receiving ends. In this section, we investigate the mechanism by which the number of rectangular coils at each end affects the coupling degree of the radial flux coupler and analyze the impact of the number of rectangular coils on the magnetic field distribution. We establish eight different radial flux coupler models in this section based on varying numbers of rectangular coils at the transmitting and receiving ends, as shown in Fig. 6.

The eight radial flux couplers have been named as Coupler T4-R2 to Coupler T10-R4, based on the number of rectangular coils at the transmitting and receiving ends. For instance, T4-R2 refers to a coupler with 4 rectangular coils at the transmitting end and 2 rectangular coils at the receiving end. All couplers have the same rectangular coil configuration with a length of 30 mm and a width of 20 mm. However, there is a difference in the distance from the center of the rectangular coils to the axis, which is 48 mm at the transmitting end and 42 mm at the receiving end. To facilitate analysis, we define the relative positions of the transmitting end and receiving end of each coupler in Fig. 6 as their initial state (0°). We define λ as the coupler's characteristic angle, and its value can be calculated using $\lambda = 360°/a$, where a represents the number of rectangular coils at the transmitting end of the coupler. For example, the characteristic angle for coupler T4-R2 and coupler T4-R4 is 90°, while the characteristic angle for coupler T6-R2 and coupler T6-R4 is 60°. This characteristic angle represents the angle at which the top rectangular coil at the receiving end rotates from the initial state (0°) to align with the neighboring rectangular coil at the transmitting end.

Finite-element software was used to calculate the variation of mutual inductance and coupling coefficient with rotation angle for different couplers and turns (where the number of turns in the transmitting and receiving coils is the same), as shown in Fig. 7(a)–(h). As seen from Fig. 7(a), the mutual inductance of coupler T4-R2 changes by one cycle when the receiving end rotates a characteristic angle (90°). The variation in mutual inductance increases with an increase in the number of turns in the rectangular coils at the transmitting and receiving ends. Negative values of mutual inductance appear when the rotation angle of the receiving end is between 20° and 70°. This is because when the rectangular coil at the receiving end rotates to the middle of the two rectangular coils at the transmitting end, the magnetic flux generated by the rectangular coils at the transmitting end passes through the receiving end in the opposite direction, causing the negative value of mutual inductance. The trend of variation in coupling coefficient with the rotation angle of the receiving end is consistent with that of mutual inductance. Fig. 7(b) shows that the variation trend of mutual inductance and coupling coefficient for Coupler T4-R4 is similar to that of coupler T4-R2. At 0°, the mutual inductance and coupling coefficient of coupler T4-R4 are larger than those of coupler T4-R2, indicating that increasing the number of rectangular coils at the receiving end increases the coupling area. When the receiving end rotates 360°, the mutual inductance of coupler T4-R2 and coupler T4-R4 changes by four cycles.

As seen in Fig. 7(c), when the receiving end rotates a characteristic angle (60°), the mutual inductance of coupler T6-R2 changes by one cycle. Compared with couplers T4-R2 and T4-R4, coupler T6-R2 has a smaller characteristic angle, which means that the receiver end of the coupler needs to undergo more mutual inductance variation cycles for a 360° rotation. As shown in Fig. 7(d), increasing the number of rectangular coils at the receiving end of coupler T6-R4 actually results in lower mutual inductance at 0° compared to coupler T6-R2. The reason for the amplitude different of mutual inductance between couplers T6-R2 and T6-R4 is that when the top rectangular coil at the receiving end of coupler T6-R4 is completely overlapped with a rectangular coil at the transmitting end, the other rectangular coil is located between the two rectangular coils at the transmitting end, as shown in Fig. 6. The magnetic flux generated by the rectangular coil at the transmitting end passes through the bottom of the receiving end rectangular coil, which partially cancels out the magnetic flux received by the fully overlapped receiving end rectangular coil, resulting in a decrease in overall mutual inductance. This phenomenon also leads to a halving of the angle corresponding to one cycle of mutual inductance variation when the receiver end of the coupler rotates, relative to its characteristic angle.

According to Fig. 7(e), when the receiving end rotates 45°, the variation in mutual inductance of coupler T8-R2 completing one cycle. Compared to couplers T4-T2 and T6-T2, the mutual inductance of coupler T8-T2 does not exhibit a significant drop below 0 during the angle variation process. According to Fig. 7(f), the mutual inductance amplitude of coupler T8-R4 is significantly improved comparing with coupler T8-R2. The angle corresponding to cycle and trend of mutual inductance variation for coupler T8-R4 are consistent with those of Coupler T8-R2. The angle corresponding to the mutual inductance variation cycle of couplers T8-R2 and T8-R4 is equal to their respective characteristic angles.

As shown in Fig. 7(g), the mutual inductance of coupler T10-R2 decreases by approximately 10% compared with coupler T8-R2 due to an increase in the number of rectangular coils at the transmitting end. When the receiving end rotates a characteristic

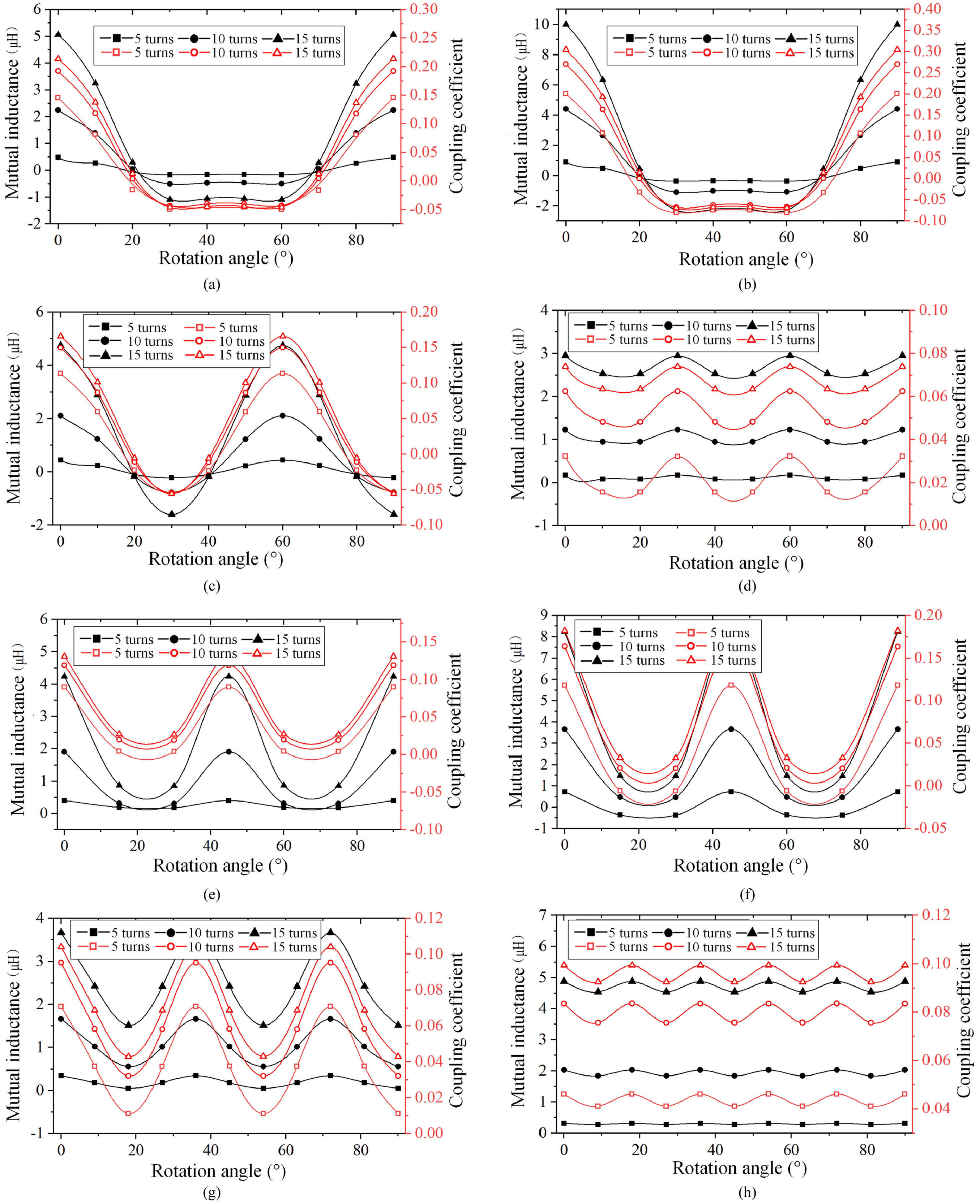

Fig. 7. Variation of mutual inductance and coupling coefficient of different couplers with rotation angle. (a) Coupler T4-R2. (b) Coupler T4-R4. (c) Coupler T6-R2. (d) Coupler T6-R4. (e) Coupler T8-R2. (f) Coupler T8-R4. (g) Coupler T10-R2. (h) Coupler T10-R4.

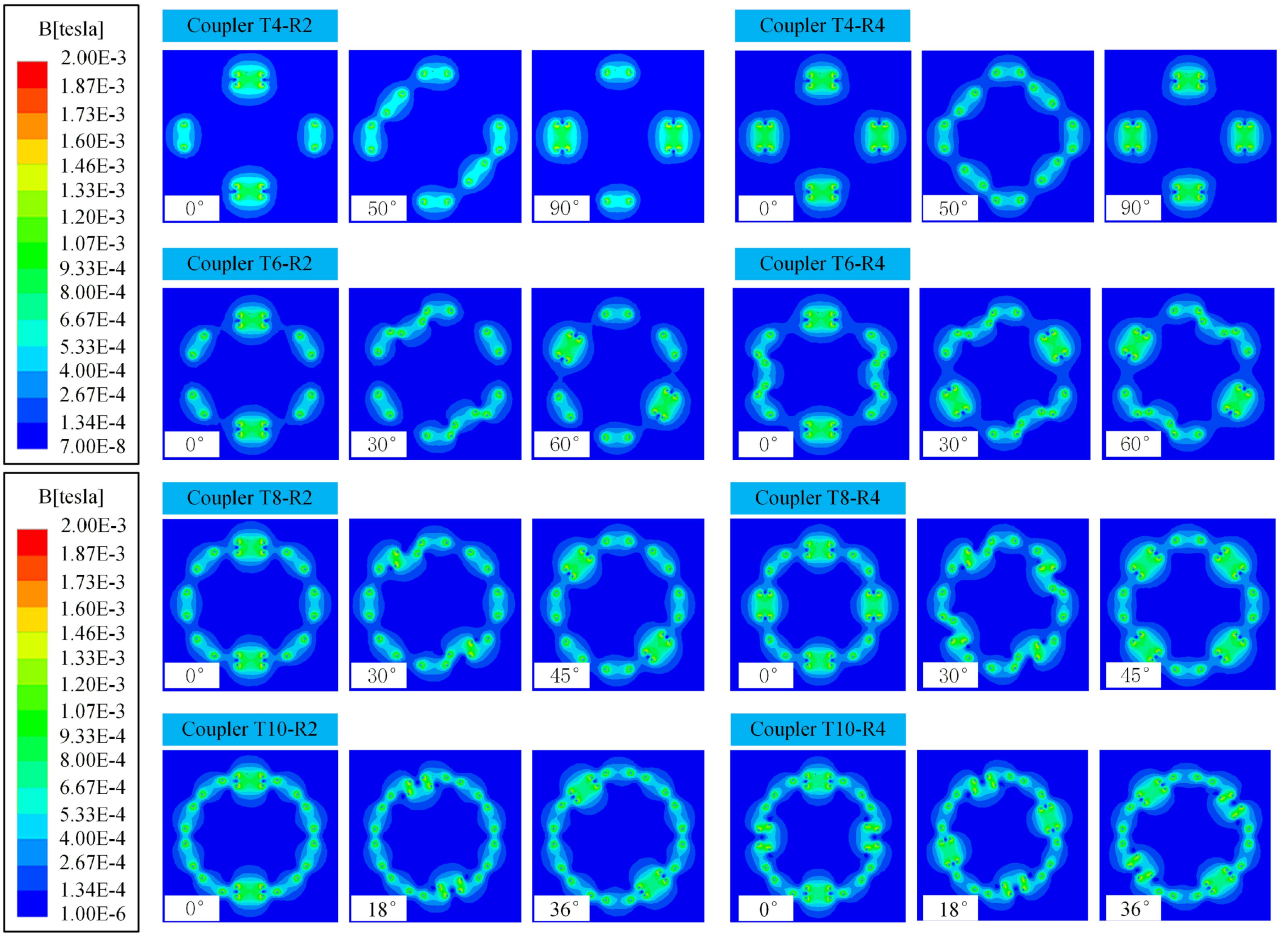

Fig. 8. Magnetic field distribution of different couplers at specific angles.

angle (36°), the change in mutual inductance of coupler T10-R2 completes one cycle. Fig. 7(h) shows that the coupler T10-R4 has the shortest cycle of mutual inductance variation, but its peak-to-peak value is less than 0.5 μH. The reason for the reduction in the angle corresponding to the mutual inductance variation cycle of the coupler T10-R4 is consistent with the coupler T6-R4.

Fig. 8 shows the magnetic field distribution of the eight types of couplers at specific angles. It can be seen from the figure that the magnetic field variation patterns of different couplers are basically consistent with their mutual inductance variation patterns, which verifies the theory of mutual inductance variation of radial flux couplers. For example, the magnetic field distribution of coupler T4-R2 at 90° is almost identical to that at 0°, they only differ in terms of their angular relationship. This 90° also corresponds to a complete cycle of mutual inductance variation. The identical magnetic fields indicates that the coupling performance of the coupler is consistent at 0° and 90°.

Among the 8 types of couplers, couplers T6-R4 and T10-R4 are quite different from the others. During the process of rotating a characteristic angle at the receiving end of the couplers, their magnetic field undergoes two complete cycles of variation, corresponding to changes in their mutual inductance. In contrast, other couplers, when rotated at the receiving end by a characteristic angle, only undergo a single cycle of magnetic field variation. For instance, for coupler T6-R4, the characteristic angle is 60°, but when the receiving end rotated 30° from the initial position (0°), it has already completed one cycle of magnetic field variation, as shown in Fig. 8. As the receiving end of this coupler continues to rotate, it will go through the next cycle of magnetic field variation. Simultaneously, during the rotation of this characteristic angle, its mutual inductance also undergoes two complete cycles of variation, as depicted in Fig. 7(d).

Special attention should be paid to the fact that in couplers T4-R2, T4-R4, T6-R2, T6-R4, T8-R4, and T10-R2, there are instances where the mutual inductance of the couplers is less than 0 μH at specific turns and angles, referred to as "reverse coupling" in this article. This means that at these specific angles, the majority of the magnetic flux generated at the transmitting end of these couplers passes through the receiving end's rectangular coil in the opposite direction (outward in the direction of the vertical axis). For the harmonic path of a rotating WPT system, reverse coupling can also transmit energy. However, this is not conducive to the controller's ability to identify the shaft's rotational speed because this reverse coupling alters the pattern of output voltage variation. Therefore, it should be avoided when designing radial flux couplers. In addition, the peak value,

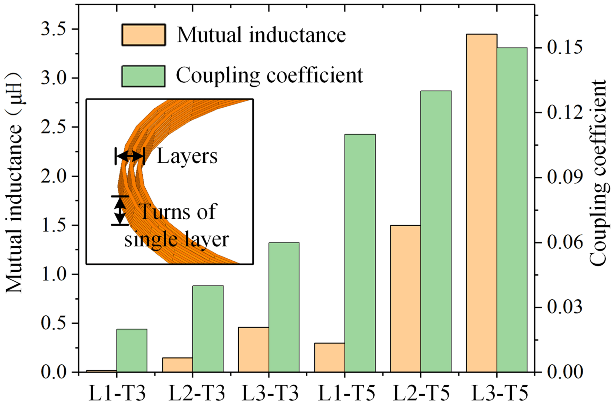

Fig. 9. Mutual inductance and coupling coefficient of different axial flux couplers.

peak-to-peak value, and the angle corresponding to one cycle of mutual inductance variation should also be closely monitored. When the peak-to-peak value of the coupler is too small as the receiving end rotates, the controller may not accurately monitor the output voltage variations in the harmonic path, leading to an inability to monitor the speed. Reducing the angle corresponding to one cycle of mutual inductance change can allow the coupler to undergo more cycles of mutual inductance change during a 360° rotation, thus improving the speed monitoring accuracy of the proposed system. The selection of the coupler's mutual inductance peak value will be discussed in conjunction with the circuit analysis in the following sections.

B. *Axial Flux Coupler*

Axial flux couplers are composed of multiple layers of helical coils. The name of the axial flux coupler is defined by the number of layers and turns. For example, L1-T3 means that the transmitting and receiving ends of the axial flux coupler are composed of a 1-layer, 3-turn coil, while L2-T3 means a 2-layer, 3-turn coil. Fig. 9 shows the mutual inductance and coupling coefficient of different axial flux couplers. The diameter of the transmitting coil used in this article is 114 mm, and the diameter of the receiving coil is 76 mm.

According to Fig. 9, for couplers with the same number of layers, the higher the number of turns, the greater the mutual inductance and coupling coefficient. For couplers with the same number of turns, the higher the number of layers, the greater the mutual inductance and coupling coefficient. The total number of turns for coupler L3-T3 is 9, while the number of turns for coupler L1-T5 is 5. The mutual inductance of coupler L3-T3 is higher than that of coupler L1-T5, but the coupling coefficient is lower than that of coupler L1-T5. It can be found that a higher number of turns does not necessarily result in a better coupling degree. In MCR-R-WPT systems, the compensation parameters, coupler parameters, and load jointly determine the output characteristics of the system. Therefore, to achieve suitable coupling performance, the number of layers and turns per layer of the axial flux coupler should be considered systematically, according to the required performance.

Fig. 10 illustrates the magnetic field distribution of various axial flux couplers. As shown in the figure, the magnetic induction intensity surrounding the coupler and the total number of turns are positively correlated. The magnetic field of the axial flux coupler is primarily distributed outside the transmitting end and inside the receiving end, and there exists a weak magnetic field region between the transmitting and receiving ends.

V. MAGNETIC SHIELD DESIGN FOR MIXED FLUX COUPLER

The magnetic properties of the metal shaft can affect the coupling state of the coupler. Therefore, it is necessary to design a magnetic shield to avoid the interference of the metal shaft on the coupling characteristics of the coupler. Redistributing the magnetic field using high magnetic permeability soft magnetic materials is a commonly used magnetic shielding method [20], [21], [22], [23], [24]. For the mixed flux couplers (T8-R4 radial flux coupler and L3-T5 axial flux coupler), ferrite was arranged around the metal shaft to reduce its impact on the coupler, as shown in Fig. 11. Fig. 11 also shows the magnetic field changes around the mixed flux coupler before and after introducing the metal shaft and before and after introducing the ferrite. It can be seen from the figure that the designed magnetic shield can effectively redistribute the magnetic field to reduce the impact of the metal shaft on the coupler.

VI. ANALYSIS OF DUAL-PATH PARALLEL COMPENSATION

The circuit topology of the dual-path parallel MCR-R-WPT system based on mixed flux coupler is illustrated in Fig. 12. The high-frequency inverter comprises a full-bridge inverter circuit composed of four N-channel MOSFETs. The compensation topologies used in the fundamental and harmonic paths are both LCC-S structures. Using LCC compensation not only ensures the stability of the output voltage of the fundamental path, but also its second-order compensation network can provide better frequency selection, allowing the inverter's fundamental component to enter the axial flux coupler and the third harmonic component to enter the radial flux coupler more effectively. The rectifier is a full-wave rectifier circuit. U_{IN} and I_{IN} denote the input voltage and input current of the high-frequency inverter, respectively. L_{P_1} and L_{S_1} refer to the transmitting coil and receiving coil of the axial flux coupler, respectively. L_{F_1}, C_{F_1}, and C_{P_1} represent the compensation inductor and compensation capacitor on the transmitting end (stationary side) of the fundamental path, respectively. C_{S_1} is the compensation capacitor on the receiving end (rotating side) of the fundamental path. R_{F_1}, R_{P_1}, and R_{S_1} are the parasitic resistances of L_{F_1}, L_{P_1}, and L_{S_1}, respectively. L_{P_2} and L_{S_2} denote the transmitting coil and receiving coil of the radial flux coupler, respectively. L_{F_2}, C_{F_2}, and C_{P_2} represent the compensation inductor and compensation capacitor on the transmitting end (stationary side) of the harmonic path, respectively. C_{S_2} is the compensation capacitor on the receiving end (rotating side) of the harmonic path. R_{F_2}, R_{P_2}, and R_{S_2} are the parasitic resistances of L_{F_2}, L_{P_2}, and L_{S_2}, respectively. C_1 and C_2 denote the filtering capacitors, and R_1 and R_2 refer to the load resistances of the

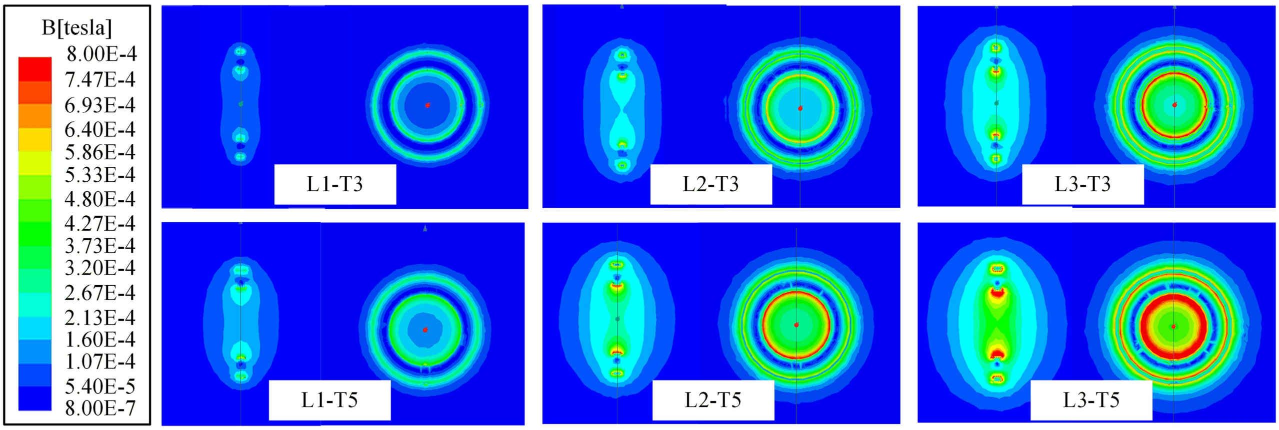

Fig. 10. Magnetic field distribution of different axial flux couplers.

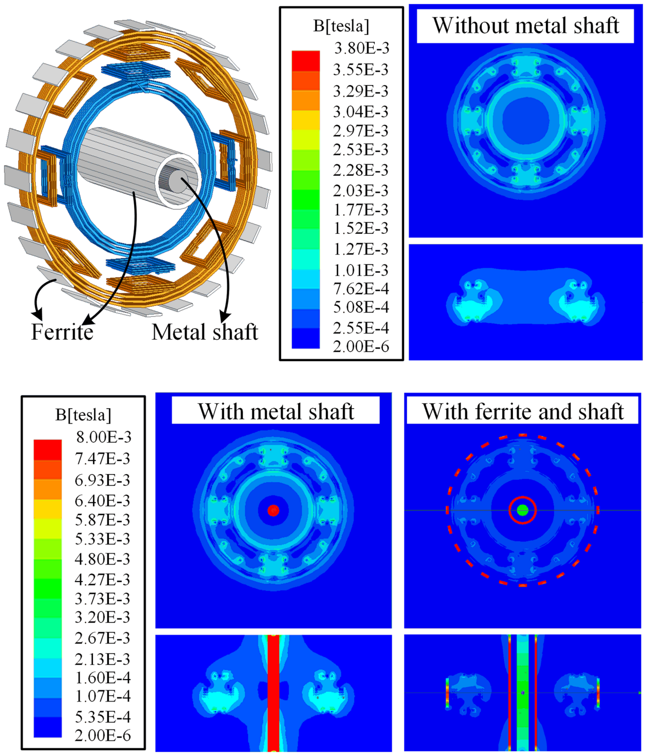

Fig. 11. Magnetic shielding of mixed flux coupler.

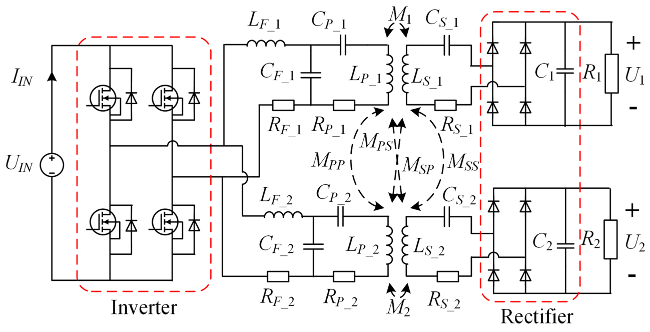

Fig. 12. System circuit topology.

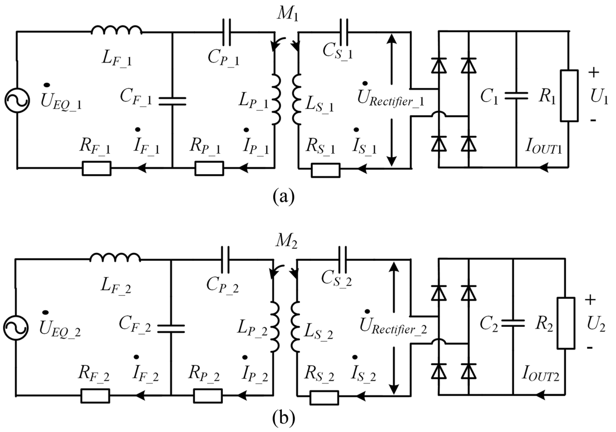

Fig. 13. Decoupled system circuit diagram. (a) Fundamental path. (b) Harmonic path.

fundamental path and harmonic path, respectively. U_1 and U_2 are the voltages across the resistors. M_1, M_2, M_{PP}, M_{PS}, M_{SP}, and M_{SS} represent the mutual inductance between coils L_{P_1}, L_{S_1}, L_{P_2}, and L_{S_2}.

As shown in Fig. 12, in the MCR-R-WPT circuit topology there are couplings in the system that require partial decoupling for analysis. The system mainly involves two types of couplings: magnetic couplings and circuit couplings. As stated earlier, self-decoupling can be achieved between radial coils and axial coils, and so M_{PP}, M_{PS}, M_{SP}, and M_{SS} can be disregarded. The present article particularly focuses on the couplings between L_{P_1} and L_{S_1}, as well as L_{P_2} and L_{S_2}. Circuit coupling refers to the coupling between the high-frequency inverter and the harmonic path and the fundamental path. To achieve circuit decoupling, the fundamental component and the harmonic component of the high-frequency inverter output voltage are extracted as the equivalent power sources for the fundamental path and the harmonic path, respectively. The decoupled system circuit is presented in Fig. 13.

In Fig. 13, $\dot{U}_{\mathrm{EQ\_1}}$ and $\dot{U}_{\mathrm{EQ\_2}}$ are the fundamental and third harmonic components, respectively, of the high-frequency inverter output voltage. $\dot{I}_{F\_1}$, $\dot{I}_{P\_1}$, $\dot{I}_{S\_1}$, and I_{OUT1} are the currents flowing through L_{F_1}, L_{P_1}, L_{S_1}, and R_1, respectively. Similarly, $\dot{I}_{F\_2}$, $\dot{I}_{P\_2}$, $\dot{I}_{S\_2}$, and I_{OUT2} are the currents flowing through L_{F_2}, L_{P_2}, L_{S_2}, and R_2, respectively. $\dot{U}_{\mathrm{Rectifier\_1}}$ and $\dot{U}_{\mathrm{Rectifier\_2}}$ are the rectifier input voltages of the fundamental path and harmonic path, respectively.

With a Fourier transform, the periodic signals can be transformed into the sum of a fundamental signal and harmonics [25]. The output signal $U_{\mathrm{EQ}}(t)$ of the high-frequency inverter can then be expressed as

$$U_{\mathrm{EQ}}(t) = \frac{4}{\pi} U_{\mathrm{IN}} \sum_{1}^{\infty} \frac{1}{2n-1} \sin(2n-1)\omega t. \tag{3}$$

The effective values of the fundamental component and third harmonic component within one period are as follows:

$$\begin{cases} \left|\dot{U}_{\mathrm{EQ\_1}}\right| = \frac{2\sqrt{2}}{\pi} U_{\mathrm{IN}} \\ \left|\dot{U}_{\mathrm{EQ\_2}}\right| = \frac{2\sqrt{2}}{3\pi} U_{\mathrm{IN}} \end{cases}. \tag{4}$$

Through decoupling, the dual-path parallel MCR-R-WPT system based on mixed flux couplers can be analyzed as two independent wireless power transfer systems. Based on the resonance characteristics of the LCC-S compensation circuit, the compensation capacitance and inductance in the system should satisfy the following relationship:

$$\begin{cases} j\omega_n L_{F\_n} + \frac{1}{j\omega_n C_{F\_n}} = 0 \\ j\omega_n L_{P\_n} + \frac{1}{j\omega_n C_{F\_n}} + \frac{1}{j\omega_n C_{P\_n}} = 0 \\ j\omega_n L_{S\_n} + \frac{1}{j\omega_n C_{S\_n}} = 0 \end{cases} \tag{5}$$

where, $n = 1, 2$ and ω_1 and ω_2 represent the resonant angular frequency of the fundamental path and harmonic path, respectively, and $3\omega_1 = \omega_2$. Using Kirchhoff's voltage law [26], the following can be obtained:

$$\begin{cases} \dot{U}_{EQ\_n} = \dot{I}_{F\_n}\left(j\omega_n L_{F\_n} + R_{F\_n}\right) \\ \quad + \left(\dot{I}_{P\_n} - \dot{I}_{F\_n}\right) \frac{1}{j\omega_n C_{F\_n}} \\ \left(\dot{I}_{P\_n} - \dot{I}_{F\_n}\right) \frac{1}{j\omega_n C_{F\_n}} = \dot{I}_{P\_n}\left(j\omega_n L_{P\_n}\right. \\ \quad \left. + \frac{1}{j\omega_n C_{P\_n}} + R_{P\_n}\right) - j\omega_n M_n \dot{I}_{S\_n} \\ j\omega_n M_n \dot{I}_{P\_n} = R_{EQ\_n} \dot{I}_{S\_n} + \dot{I}_{S\_n}\left(j\omega_n L_{S\_n}\right. \\ \quad \left. + \frac{1}{j\omega_n C_{S\_n}} + R_{S\_n}\right) \end{cases} \tag{6}$$

where, $n = 1, 2$. R_{EQ_n} is the equivalent resistance of the fundamental path and harmonic path, which is given by

$$R_{\mathrm{EQ}\_n} = \frac{8}{\pi^2} R_n \tag{7}$$

where $n = 1, 2$.

The equivalent impedance of the receiving end of the fundamental wave path can be determined from

$$Z_{\mathrm{REC\_1}} = j\omega_1 L_{S\_1} + \frac{1}{j\omega_1 C_{S\_1}} + R_{S\_1} + R_{\mathrm{EQ\_1}}. \tag{8}$$

The impedance from the receiving end of the fundamental wave path to the transmitting end can be calculated using

$$Z_{M\_1} = \frac{{\omega_1}^2 {M_1}^2}{Z_{\mathrm{REC\_1}}}. \tag{9}$$

The impedance of transmitting end in the fundamental wave path can be calculated from

$$\begin{aligned} Z_{\mathrm{TRA\_1}} = & \left(\frac{1}{j\omega_1 C_{P\_1}} + j\omega_1 L_{P\_1} + Z_{M\_1} + R_{P\_1}\right) \parallel \frac{1}{j\omega_1 C_{F\_1}}. \\ & + j\omega_1 L_{F\_1} + R_{F\_1} \end{aligned} \tag{10}$$

Similarly, the impedance of transmitting end in the harmonic path can be calculated using

$$\begin{aligned} Z_{\mathrm{TRA\_2}} = & \left(\frac{1}{j\omega_2 C_{P\_2}} + j\omega_2 L_{P\_2} + Z_{M\_2} + R_{P\_2}\right) \parallel \frac{1}{j\omega_2 C_{F\_2}}. \\ & + j\omega_2 L_{F\_2} + R_{F\_2} \end{aligned} \tag{11}$$

By combining (5) to (11), the total input impedance of the system can be obtained as

$$Z_{\mathrm{TOTAL}} == Z_{\mathrm{TRA\_1}} \parallel Z_{\mathrm{TRA\_2}}. \tag{12}$$

When the fundamental and harmonic paths are resonating independently, the values of $\dot{I}_{F\_1}$, $\dot{I}_{S\_1}$, $\dot{I}_{F\_2}$, and $\dot{I}_{S\_2}$ can be obtained using

$$\begin{cases} \dot{I}_{F\_n} = \frac{[(\omega_n M_n)^2 + R_{P\_n}(R_{S\_n} + R_{\mathrm{EQ}\_n})]\dot{U}_{\mathrm{EQ}\_n}}{(\omega_n L_{F\_n})^2 (R_{S\_n} + R_{\mathrm{EQ}\_n})} \\ \dot{I}_{S\_n} = \frac{M_n \dot{U}_{\mathrm{EQ}\_n}}{L_{F\_n}(R_{S\_n} + R_{\mathrm{EQ}\_n})} \end{cases} \tag{13}$$

where $n = 1, 2$.

In addition, the fundamental path output power P_1, the harmonic wave path output power P_2, the total efficiency η of the system ignoring inverter and rectifier losses (η is the ratio of the sum of the fundamental path output power P_1 and the harmonic path output power P_2 to the total input power), and power transfer efficiency η_1 ignoring inverter and rectifier losses (η_1 is the ratio of the fundamental path output power P_1 to the total input power) can be calculated from

$$\begin{cases} P_n = \left|\dot{I}^2_{S\_n} R_{\mathrm{EQ}\_n}\right| \qquad (n = 1, 2) \\ \eta = \frac{P_{\mathrm{OUT}}}{P_{\mathrm{IN}}} = \frac{P_1 + P_2}{{U_{\mathrm{EQ}}}^2 / Z_{\mathrm{TOTAL}}} \\ \eta_1 = \frac{P_1}{P_{\mathrm{IN}}} = \frac{P_1}{{U_{\mathrm{EQ}}}^2 / Z_{\mathrm{TOTAL}}} \end{cases}. \tag{14}$$

When the parasitic resistance of the coil is ignored, the voltage-current gain expressions for the fundamental and harmonic paths can be obtained using

$$\begin{cases} G_{U\_n} = \left|\frac{\dot{I}_{S\_n} R_{\mathrm{EQ}\_n}}{\dot{U}_{\mathrm{EQ}\_n}}\right| = \frac{M_n}{L_{F\_n}} \\ G_{I\_n} = \left|\frac{\dot{I}_{S\_n}}{\dot{I}_{F\_n}}\right| = \frac{L_{F\_n}}{M_n} \end{cases} \quad (n = 1, 2)\ . \tag{15}$$

According to (15), it is evident that the voltage gains G_{U_1} and G_{U_2} are independent of the load, allowing the system to maintain a constant voltage output capability. Moreover, the mutual inductance is positively correlated with the voltage gain. A reasonable coupler design can keep M_1 constant while allowing M_2 to vary periodically with the rotation of the rotor,

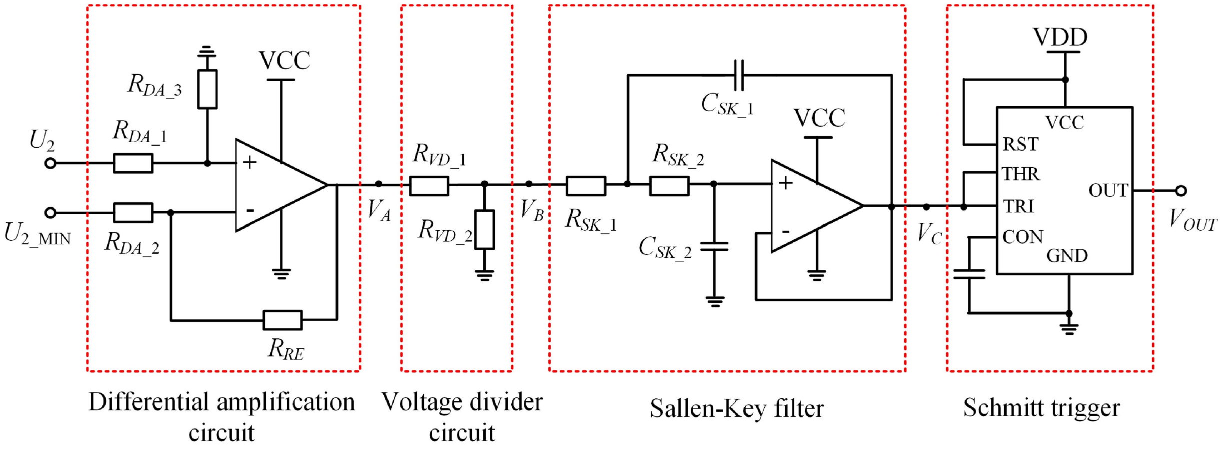

Fig. 14. Signal processing circuit.

which in turn keeps G_{U_1} constant while causing G_{U_2} to vary periodically with rotor rotation. By monitoring the periodic changes in the output voltage, it is feasible to deduce changes in mutual inductance and, therefore, speed variation.

Combining (13) to (15), it can be observed that M_1 and M_2 only affect the output voltage and output power of their respective paths. This means that when the system uses varying M_2 for speed monitoring, it will not have an impact on the output voltage and power of the fundamental path.

Combining (13) and (14), M_1 is positively correlated with P_1, while L_{F_1} is negatively correlated with the P_1. M_2 is positively correlated with P_2, while L_{F_2} is negatively correlated with P_2. For the fundamental path, its primary task is to provide power to the rotating load, whereas for the harmonic path, its primary task is to obtain speed characteristics by utilizing the output characteristics. Higher power on the harmonic path can lead to lower system transfer efficiency η_1. Therefore, for the fundamental path, M_1 and L_{F_1} should be chosen appropriately based on power requirements to ensure stable supply of power. For the harmonic path, M_2 should be reduced and L_{F_2} increased appropriately to reduce losses in the harmonic path.

VII. SIGNAL PROCESSING

The previous section indicated that there is a proportional relationship between the output voltage gain G_{U_2} and the mutual inductance M_2, in the harmonic path. The variation in G_{U_2}, caused by changes in M_2, cannot be directly recognized as a speed signal. In this section, a signal processing circuit as shown in Fig. 14 is employed to generate a speed signal that can be read by the controller.

In Fig. 14, the harmonic path output voltage U_2 is collected through a differential amplification circuit, and a voltage divider circuit is employed to control its maximum and minimum values around 5 and 0 V, respectively. The signal is then filtered through a Sallen-key filter to remove high-frequency components, and a Schmitt trigger based on 555-timer generates a pulse signal that can be captured by the controller. Finally, the speed is obtained by counting the pulses per unit time.

In Fig. 14, when $R_{\text{DA\_1}} = R_{\text{DA\_2}}$ and $R_{\text{DA\_3}} = R_{\text{RE}}$, the input voltage V_A of the differential amplification circuit can be calculated using:

$$V_A = \frac{R_{\text{RE}}}{R_{\text{DA\_2}}} \left(U_2 - U_{2\_\text{MIN}}\right). \tag{16}$$

The input voltage V_B of the voltage divider circuit can be calculated using

$$V_B = \frac{R_{\text{VD\_2}}}{R_{\text{VD\_1}} + R_{\text{VD\_2}}} V_A. \tag{17}$$

The transfer function of the Sallen-key filter is given by

$$\frac{V_C(s)}{V_B(s)} = \frac{(2\pi f_0)^2}{s^2 + \frac{1}{Q}(2\pi f_0)\, s + (2\pi f_0)^2} \tag{18}$$

where f_0 is the cutoff frequency of the filter, and Q is the quality factor, calculated from

$$\begin{cases} f_0 = \frac{\omega_0}{2\pi} = \frac{1}{2\pi\sqrt{R_{SK\_1}R_{SK\_2}C_{SK\_1}C_{SK\_2}}} \\ Q = \frac{\sqrt{R_{SK\_1}R_{SK\_2}C_{SK\_1}C_{SK\_2}}}{(R_{SK\_1}+R_{SK\_2})C_{SK\_2}} \end{cases}. \tag{19}$$

In the 555-timer based Schmitt trigger, its two trigger voltages are 1/3 V_{DD} and 2/3 V_{DD}, respectively. When V_C transitions from high to low through 1/3 V_{DD}, V_{OUT} produces a rising edge, and when V_C transitions from low to high through 2/3 V_{DD}, V_{OUT} generates a falling edge. The upper limit on the number of triggers per minute for the Schmidt trigger is determined by the 555-timer, which has a maximum operating frequency of 300 kHz. This is sufficient to ensure the effective fulfillment of speed measurement requirements for most types of rotating equipment.

VIII. EXPERIMENT

To study the performance of the dual-path parallel MCR-R-WPT system based on the mixed flux coupler, as proposed in this article, a rotating experimental platform was constructed. The radial flux coupler in the mixed flux coupler adopts coupler T8-R4 of Fig. 6, with a turn ratio of 10 turns, while the axial flux coupler adopts the coupler type L3-N5 of Fig. 9, with a turn ratio

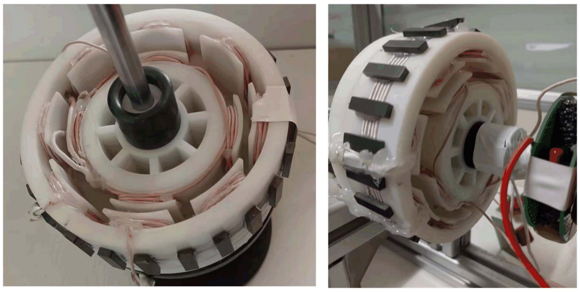

Fig. 15. Mixed flux coupler prototype.

TABLE II
PARAMETERS OF MIXED FLUX COUPLER

Symbol	Content	Value
L_{P_1}	Self-inductance of axial flux coupler transmitter	56.78 μH
L_{S_1}	Self-inductance of axial flux coupler receiver	23.99 μH
M_1	Mutual inductance of axial flux coupler	12.06 μH
L_{P_2}	Self-inductance of radial flux coupler transmitter	32.27 μH
L_{S_2}	Self-inductance of radial flux coupler receiver	17.27 μH
$M_2(0°)$	Mutual inductance of radial flux coupler (0°)	3.02 μH
$M_2(22.5°)$	Mutual inductance of radial flux coupler (22.5°)	1.26 μH

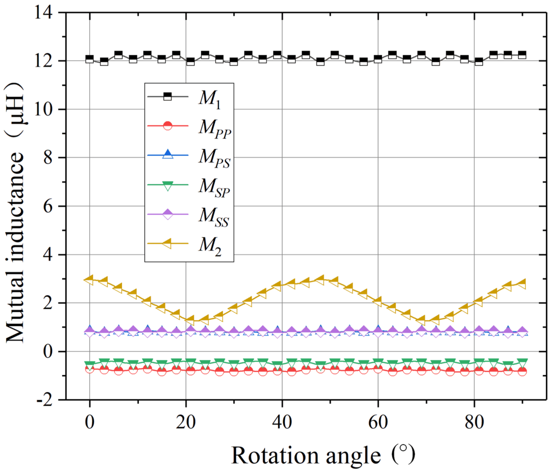

Fig. 16. Mutual inductance between axial flux coupler and radial flux coupler.

of 15 turns. The prototype of the mixed flux coupler is shown in Fig. 15, and the electrical parameters are given in Table II.

When the mixed flux coupler rotates, the mutual inductance between each coil is measured every 3°, as shown in Fig. 16. It can be seen from the Fig. 16 that the maximum mutual inductance between the transmitter and the receiver of the axial flux coupler is 12.06 μH, and it does not change with the rotation angle; the maximum mutual inductance the radial flux coupler occurs at 0° rotation angle, with a maximum value of 3.02 μH, and the minimum value of 1.26 μH occurs at 22.5°. Therefore, it can be inferred that the mutual inductance of the radial flux coupler will undergo eight periodic changes when the shaft rotates 360°. In addition, the mutual inductance between the transmitter of the axial flux coupler and the transmitter and receiver of the radial flux coupler are relatively low, and the same holds for the receiver of the axial flux coupler. These couplings remain relatively stable and achieve decoupling between each other. To sum up, the mixed flux coupler proposed in this article satisfies the requirements of the dual-path parallel MCR-R-WPT system.

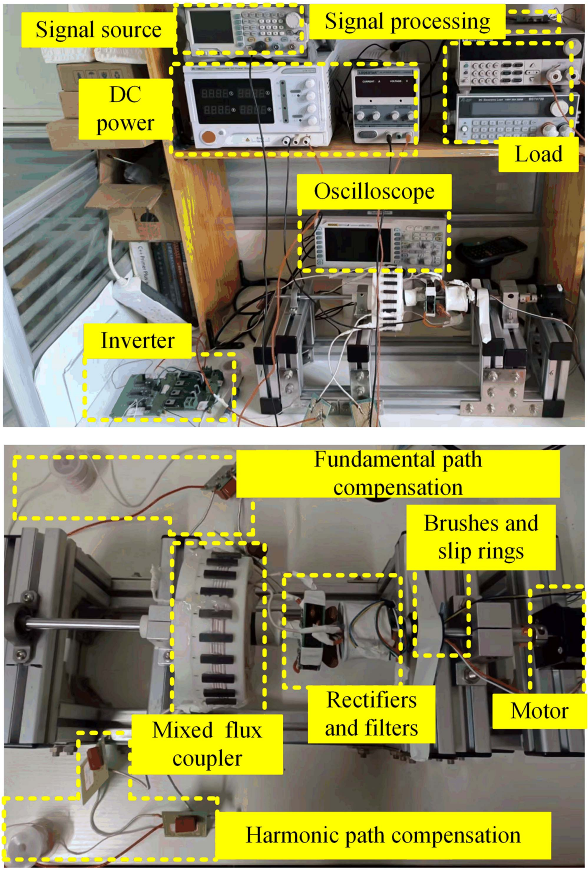

Fig. 17. Prototype of a dual-path parallel MCR-R-WPT system based on a mixed flux coupler.

Fig. 17 shows the test setup for the prototype dual-path parallel MCR-R-WPT system based on a mixed flux coupler. The compensation parameters used in the prototype are given in Table III. The full-bridge inverter is composed of four MOSFETs and is driven by two IR2110s. The inverter control signal is generated by a signal source. Both the fundamental and harmonic paths in the prototype are connected to the output of the inverter, which has an input voltage of 36 V and operating frequency of 100 kHz. The output currents of the fundamental and harmonic paths are sent to a programmable electronic load via slip rings.

To begin with, the key waveforms of the system were tested while stationary to verify the resonant state of the fundamental and harmonic paths, as shown in Fig. 18(a)–(f). The fundamental path load, R_1, and harmonic path load, R_2, are both 5 Ω.

TABLE III
PARAMETERS OF COMPENSATION

Symbol	Content	Value
L_{F_1}	Compensation inductance at the transmitter of fundamental path	13.63 μH
C_{F_1}	Compensation capacitor at the transmitter of fundamental path	185.73 nF
C_{P_1}	Compensation capacitor at the transmitter of fundamental path	585.52 nF
C_{S_1}	Compensation capacitor at the receiver of fundamental path	106.66 nF
L_{F_2}	Compensation inductance at the transmitter of harmonic path	9.68 μH
C_{F_2}	Compensation capacitor at the transmitter of harmonic path	288.81 nF
C_{P_2}	Compensation capacitor at the transmitter of harmonic path	125.05 nF
C_{S_2}	Compensation capacitor at the receiver of harmonic path	162.97 nF

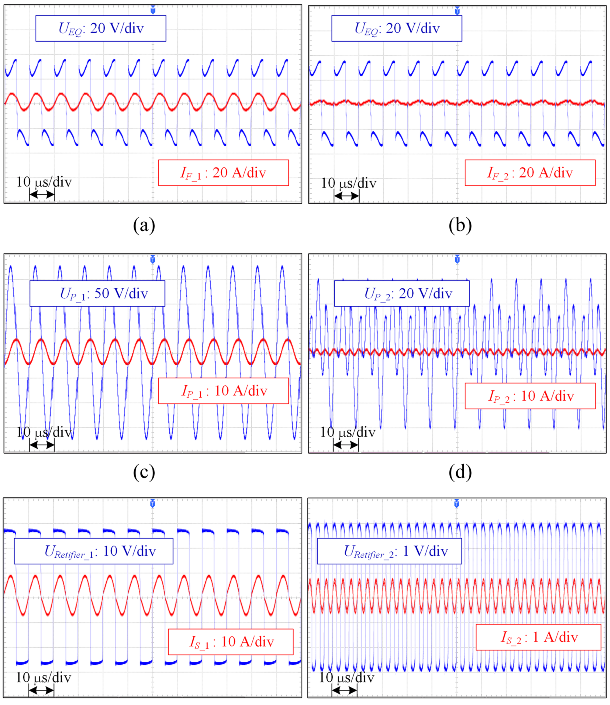

(a) (b)

(c) (d)

(e) (f)

Fig. 18. System state key waveforms at 0°. (a) U_{EQ} and I_{F_1}. (b) U_{EQ} and I_{F_2}. (c) U_{P_1} and I_{P_1}. (d) U_{P_2} and I_{P_2}. (e) $U_{\mathrm{Retifier\_1}}$ and I_{S_1}. (f) $U_{\mathrm{Retifier\_2}}$ and I_{S_2}.

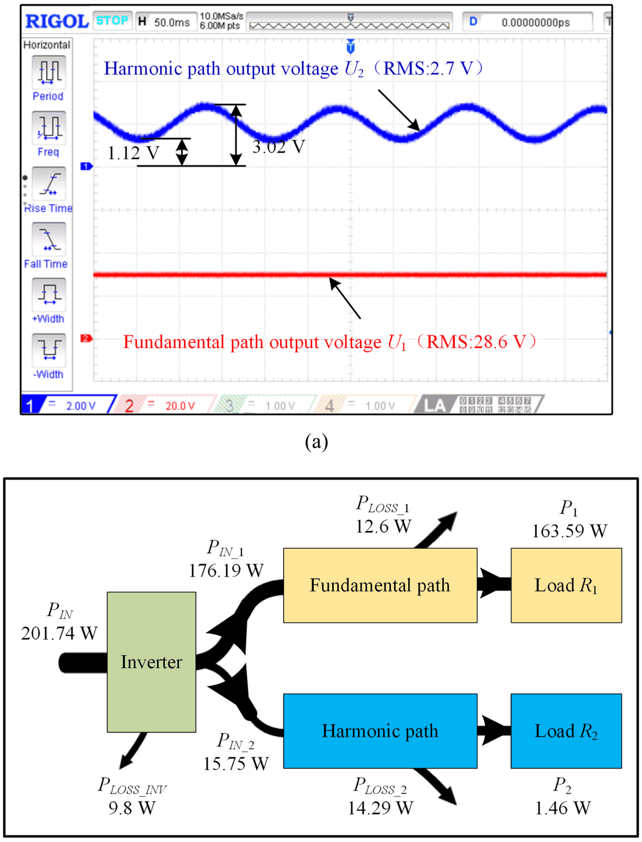

(a)

(b)

Fig. 19. System output voltage waveforms at 50 r/min and power flow analysis. (a) Output voltage waveforms. (b) Power flow analysis.

Comparing Fig. 18(a) and (b), it can be observed that both inductor current I_{F_1} and I_{F_2} are composed of fundamental and harmonic components, but the latter's harmonic components are greater than the former. The effective value of I_{F_1} is much larger than that of I_{F_2}, indicating that the output power of the inverter is mainly utilized for rotating wireless power transmission, and the energy consumed for speed monitoring based on the harmonic path is relatively small. From Fig. 18(c), it can be observed that the current I_{P_1} flowing through the transmitting end of the axial flux coupler and its voltage U_{P_1} exhibit good sinusoidal characteristics, and both their frequency variations match the fundamental frequency of the inverter output. From Fig. 18(d), it can be seen that the current I_{P_2} flowing through the transmitting end of the radial flux coupler and its voltage U_{P_2} show a superposition of the third harmonic component and the fundamental component, mainly dominated by the third harmonic. This means that the radial flux coupler is operating in a third harmonic state at this moment. Comparing Fig. 18(e) and (f), it can be observed that the changing trends of the input current I_{S_1} and input voltage $U_{\mathrm{Retifier\_1}}$ of the fundamental path rectifier are identical to the input current I_{S_2} and input voltage $U_{\mathrm{Retifier\_2}}$ of the harmonic path rectifier, respectively. They only differ in frequency and amplitude. Clearly, the resonance frequency of the latter is three times that of the former, indicating that the dual-path compensation proposed in this article is functioning properly.

The rotating wireless power transmission of the system was verified, when the motor speed was set to 50 r/min, and the fundamental path load R_1 and harmonic path load R_2 were both 5 Ω. The voltage output waveforms of the fundamental and harmonic paths were observed, and a power flow analysis was conducted, as shown in Fig. 19(a) and (b), respectively. In Fig. 19(b), P_{IN} represents the total power flowing into the system; $P_{\mathrm{IN\_1}}$ and $P_{\mathrm{IN\_2}}$ represent the power flowing into the fundamental and harmonic paths, respectively; P_1 and P_2 represent the power flowing through loads R_1 and R_2, respectively; $P_{\mathrm{LOSS\_INV}}$, $P_{\mathrm{LOSS\_1}}$, and $P_{\mathrm{LOSS\_2}}$ represent the losses in the inverter, fundamental path, and harmonic path, respectively.

From Fig. 19(a), it can be seen that the effective value of the output voltage of the fundamental path was 28.6 V, and the output power of the system was 163.59 W. The maximum and minimum values of the harmonic output voltage were 3.02 and 1.12 V, respectively, with an effective value of 2.7 V and power of 1.46 W. From Fig. 19(b), it can be observed that the inverter losses account for approximately 4.85% of the input power. Regarding the power output from the inverter, 91.79% is directed into the fundamental path, while the remaining portion enters the harmonic path. The system's power transmission efficiency η_1 is 81.08%, and the overall useful power efficiency η is 81.81%. The losses in the fundamental and harmonic paths are 12.6 and 14.29 W, respectively. The primary reasons for the higher losses in the harmonic path are twofold: first, the higher frequency in the harmonic path leads to significant eddy current losses in the coils, and secondly, the coupling degree of the radial flux coupler in the harmonic path is relatively low. Therefore, it can be concluded that the system can stably achieve wireless power transmission from the stationary end to the rotating end.

To validate the system's speed measurement function, the motor speed was first set within the range of 50 to 250 r/min and then the output waveform of the harmonic path was measured at different speeds. By comparing the calculated speed from the output voltage waveform of the harmonic path with the preset speed, the speed measurement function was successfully verified. Fig. 20(a)–(c) shows the harmonic path output voltage waveforms at different predicted speeds, while the signal processing circuit is validated in Fig. 20(a).

Fig. 20(a) shows that when the preset speed was 50 r/min, the output voltage waveform of the harmonic path changed its period every 150 ms, requiring eight periods to complete one rotation, and the total time was 1.2 s. Therefore, the measured value of the shaft speed was 50 r/min, which was equal to the preset speed. What's more, when the output voltage of the harmonic path passes through the signal processing circuit, a square wave with the same frequency as the original signal can be generated, making it convenient for the controller to capture. Similarly, it can be seen from the Fig. 20(b) and (c) that when the preset speeds were 150 and 250 r/min, the rotation periods calculated from the voltage waveform were 400 and 240 ms, respectively. The measured speeds calculated based on the periods were equal to their respective preset speeds. In summary, measuring the shaft speed based on the period changes of the harmonic path voltage waveform is a realistic method.

To verify the influence of the fundamental path load and the harmonic path load on the system, the system's output power and efficiency were tested under different loads at a rotation angle of 0°. Fig. 21 illustrates the system's power transmission efficiency η_1 under different loads.

From Fig. 21, it can be known that the power transmission efficiency η_1 exhibits slight fluctuations with the load variation but remains above 80% overall.

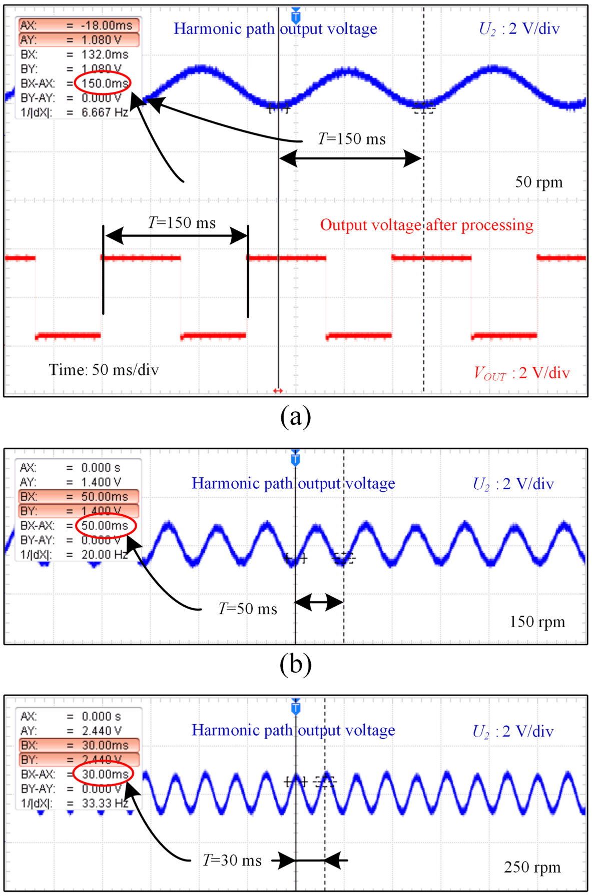

(a)

(b)

(c)

Fig. 20. Output voltage waveform of harmonic path at different rotational speeds. (a) 50 r/min. (b) 150 r/min. (c) 250 r/min.

Fig. 22(a)–(d) shows the output voltage and power under different loads at a rotation angle of 0°. As shown in Fig. 22(a), the output voltage of the fundamental path decreases with the reduction of the load, but the decrease is relatively small. The load variation of the harmonic path has little effect on the output voltage of the fundamental path. Similarly, as shown in Fig. 22(b), the load of the harmonic path has little effect on the output power of the fundamental path. As shown in Fig. 22(c) and (d), the output voltage and power of the harmonic path are only affected by the load of the harmonic path. In summary, the load variation of the fundamental path and the harmonic path only affects the performance of their respective branches. Therefore, it can be inferred that the variation of the fundamental path load in practical applications has little impact on the harmonic path, which ensures the stable operation of speed monitoring using the output voltage variation of the harmonic path.

IX. CONCLUSION

This article has presented a MCR-R-WPT system based on a mixed flux coupler and a dual-path parallel compensation topology, which achieves both rotational power transmission and

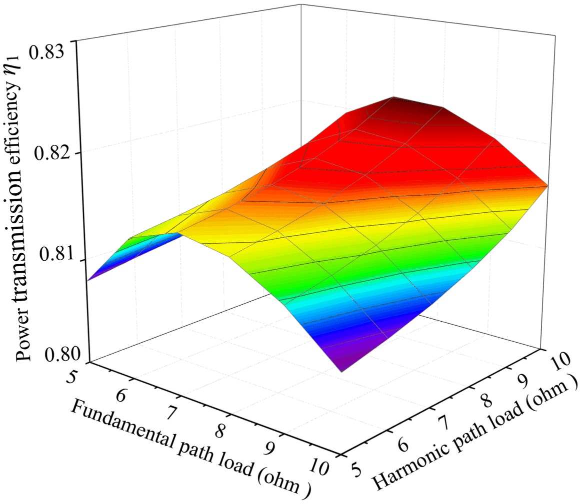

Fig. 21. Power transmission efficiency under different loads.

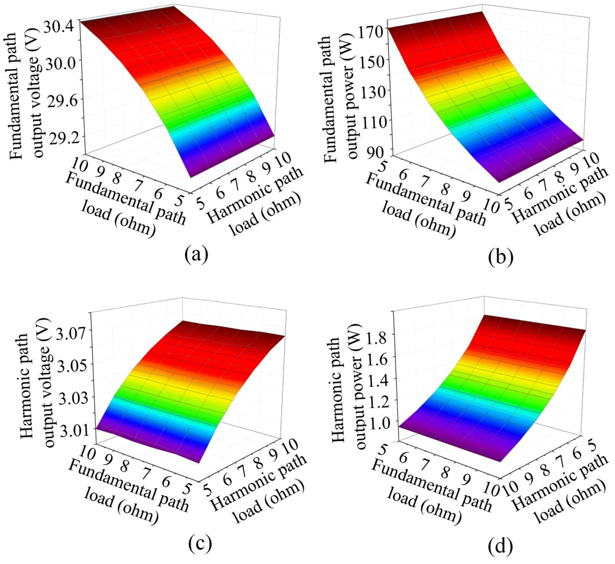

(a) (b)

(c) (d)

Fig. 22. Output voltage and power of the system at different loads. (a) Fundamental path output voltage. (b) fundamental path output power. (c) Harmonic path output voltage. (d) Harmonic path output power.

speed detection. For the mixed flux coupler, its rotational characteristics and structural properties have been analyzed, and optimization has been conducted from the perspectives of coupling degree and magnetic field distribution. The output characteristics and voltage gain formula of the MCR-R-WPT system based on dual-path parallel compensation have been derived. Design guidelines have been provided for different branches to fulfill their respective functions optimally. A prototype of the rotational wireless power transfer system based on the mixed flux coupler and the dual-path parallel compensation has been built and tested through experiments of rotation wireless power transfer, speed measurement, and load perturbation. The following conclusions can be made.

1) The mixed flux coupler proposed in this article can basically achieve self-decoupling of radial and axial flux. The coupling degree of the axial flux coupler remains stable, while the coupling degree of the radial flux coupler is related to the rotation angle of the axis and the number of rectangular coils.
2) The proposed system can achieve both stable wireless power transfer and accurate speed measurement in harsh environments. The maximum transmission power of the system can reach 163.59 W, and the system power transmission efficiency remains above 80% when the dual-load is between 5 and 10 ohms.
3) Perturbations in the fundamental load branch do not affect the output characteristics of the harmonic load branch.

REFERENCES

[1] K. Fischer et al., “Reliability of power converters in wind turbines: Exploratory analysis of failure and operating data from a worldwide turbine fleet,” *IEEE Trans. Power Electron.*, vol. 34, no. 7, pp. 6332–6344, Jul. 2019.

[2] W. Huang et al., “Tool wear in ultrasonic vibration–assisted drilling of CFRP: A comparison with conventional drilling,” *Int. J. Adv. Manuf. Technol.*, vol. 115, no. 5, pp. 1809–1820, May 2021.

[3] W. Huang, S. Cao, Q. Zhou, and C. Wu, “Tool breakage monitoring based on sequential hypothesis test in ultrasonic vibration-assisted drilling of CFRP,” *Int. J. Adv. Manuf. Technol.*, vol. 124, no. 7/8, pp. 118–129, Jul. 2022.

[4] W. Huang, X. Zhang, C. Wu, S. Cao, and Q. Zhou, “Tool wear prediction in ultrasonic vibration-assisted drilling of CFRP: A hybrid data-driven physics model-based framework,” *Tribol. Int.*, vol. 174, 2022, Art. no. 107755.

[5] X. Qiao, S. Niu, J. Lin, M. Chen, and Y. Wu, “A novel magnetically coupled resonant wireless power transfer technique used in rotary ultrasonic machining process,” in *Proc. IEEE Wireless Power Transfer Conf.*, 2021, pp. 1–4.

[6] J. M. Aitken et al., “Simultaneous localization and mapping for inspection robots in water and sewer pipe networks: A review,” *IEEE Access*, vol. 9, pp. 140173–140198, 2021.

[7] H. Saneie, Z. Nasiri-Gheidari, and F. Tootoonchian, “Structural design and analysis of a high reliability multi-turn wound-rotor resolver for electric vehicle,” *IEEE Trans. Veh. Technol.*, vol. 69, no. 5, pp. 4992–4999, May 2020.

[8] R. Yazdanpanah, S. A. Mortazavizadeh, Y. Teng, O. Anaya-Lara, and D. Campos-Gaona, “An integrated rotary transformer and 3-phase dual-active-bridge converter for high power transfer in novel X-rotor wind turbines,” in *Proc. IEEE Int. Magn. Conf.*, 2023, pp. 1–5.

[9] Y. Zhou, Y. Luo, S. Liu, and D. Li, “An efficient and stable embedded multi-U-shaped column rotary transformer,” *IEEE Trans. Power Electron.*, vol. 38, no. 5, pp. 6734–6743, May 2023.

[10] D. Wang et al., “Redundancy and fault-tolerant design of rotational MIMO wireless power transfer system,” in *Proc. IEEE Veh. Power Propulsion Conf.*, 2021, pp. 1–6.

[11] Z. Yan, B. Song, Y. Zhang, K. Zhang, Z. Mao, and Y. Hu, “A rotation-free wireless power transfer system with stable output power and efficiency for autonomous underwater vehicles,” *IEEE Trans. Power Electron.*, vol. 34, no. 5, pp. 4005–4008, May 2019.

[12] M. Pang, K. Xiang, J. Lu, and W. Yue, “Analysis and design of wireless power transfer system for robot joints,” in *Proc. IEEE 5th Int. Elect. Energy Conf.*, 2022, pp. 1826–1830.

[13] K. Song et al., “A rotation-lightweight wireless power transfer system for solar wing driving,” *IEEE Trans. Power Electron.*, vol. 34, no. 9, pp. 8816–8830, Sep. 2019.

[14] T. Wang, Y. Yan, L. Wang, and Y. Hu, “Rotational speed measurement through image similarity evaluation and spectral analysis,” *IEEE Access*, vol. 6, pp. 46718–46730, 2018.

[15] L. Wang, J. Li, H. Chen, and Z. Pan, “Radial-flux rotational wireless power transfer system with rotor state identification,” *IEEE Trans. Power Electron.*, vol. 37, no. 5, pp. 6206–6216, May 2022.

[16] G. Fracastoro and E. Magli, “Steerable discrete Fourier transform,” *IEEE Signal Process. Lett.*, vol. 24, no. 3, pp. 319–323, Mar. 2017.

[17] C. Cai, J. Wang, Y. Luo, M. Xue, Y. Hong, and C. Wang, “Self-decoupling and active-shielding coils of dual-rectangle-coil transmitters for wireless charging area extension,” in *Proc. IEEE 20th Biennial Conf. Electromagn. Field Comput.*, 2022, pp. 1–2.

[18] J. Yi, P. Yang, Z. Li, P. Kong, and J. Li, "Mutual inductance calculation of circular coils for an arbitrary position with a finite magnetic core in wireless power transfer systems," *IEEE Trans. Transp. Electrific.*, vol. 9, no. 1, pp. 1950–1959, Mar. 2023.

[19] P. Lin, N. Zhang, M. Chang, and L. Xu, "Research on the model and the location method of ship shaft-rate magnetic field based on rotating magnetic dipole," *IEEE Access*, vol. 8, pp. 162999–163005, 2020.

[20] T. Wang, W. Yuan, D. Fu, and J. Yuan, "Improvement of magnetic shielding for transformers based on the magnetic flux characteristics at shielding ends," *IEEE Trans. Magn.*, vol. 56, no. 1, Jan. 2020, Art. no. 7501804.

[21] G. Rituraj and P. Kumar, "A new magnetic structure of unipolar rectangular coils in WPT systems to minimize the ferrite volume while maintaining maximum coupling," *IEEE Trans. Circuits Syst. II, Exp. Briefs*, vol. 68, no. 6, pp. 2072–2076, Jun. 2021.

[22] K. Song et al., "A review on interoperability of wireless charging systems for electric vehicles," *Energies*, vol. 16, no. 4, 2023, Art. no. 1653.

[23] Z. Dai and J. Wang, "A dual-frequency WPT based on multilayer self-decoupled compact coil and dual CLCL hybrid compensation topology," *IEEE Trans. Power Electron.*, vol. 37, no. 11, pp. 13955–13965, Nov. 2022.

[24] Z. Dai et al., "Magnetic coupling mechanism with omnidirectional magnetic shielding for wireless power transfer," *IEEE Trans. Electromagn. Compat.*, vol. 65, no. 5, pp. 1565–1574, Oct. 2023.

[25] C. Eleftheriadis and G. Karakonstantis, "Energy-efficient fast Fourier transform for real-valued applications," *IEEE Trans. Circuits Syst. II, Exp. Briefs*, vol. 69, no. 5, pp. 2458–2462, May 2022.

[26] R. Drummond, L. D. Couto, and D. Zhang, "Resolving Kirchhoff's laws for parallel li-ion battery pack state-estimators," *IEEE Trans. Control Syst. Technol.*, vol. 30, no. 5, pp. 2220–2227, Sep. 2022.

Longyang Wang received the B.Eng. degree in 2017 from the Wuhan University of Technology, Wuhan, China, where he is currently working toward the Ph.D. degree with the School of Mechanical and Electronic Engineering.

His research interests include wireless transmission technology based on magnetic resonance, linear motor, and system equipment for transmission and distribution.

Jiangui Li was born in Shanxi, China, in 1983. She received the Ph.D. degree from the Department of Electrical and Electronic Engineering, The University of Hong Kong, Hong, Kong.

In 2012, she joined the University of Michigan, Ann Arbor, MI, USA, as a Postdoctoral Researcher. She is currently a Professor with the School of Mechanical and Electronic Engineering, Wuhan University of Technology, Wuhan, China. Her research interests include wireless charging, electric motor, and renewable energy power generation.

Guangbin Luo was born in Fujian, China, in 1999. He received the B.Eng. degree in 2021 from the Wuhan University of Technology, Wuhan, China, where he is currently working toward the M.A.Eng. degree with the School of Mechanical and Electronic Engineering.

His research focuses on wireless transmission technology based on magnetic resonance.

Qinghe Si was born in Henan, China, in 1998. He received the B.Eng. degree from the Tiangong University, Tianjin, China, in 2020. He is currently working toward the M.A.Eng. degree with the School of Mechanical and Electronic Engineering, Wuhan University of Technology, Wuhan, China.

His research focuses on wireless transmission technology based on magnetic resonance.

Zheyuan Guo was born in Shandong, China, in 2000. He received the B.Eng. degree in 2022 from the Wuhan University of Technology, Wuhan, China, where he is currently working toward the M.A.Eng. degree with the School of Mechanical and Electronic Engineering.

His research focuses on include wireless transmission technology based on magnetic resonance.

Yinchong Peng was born in Henan, China, in 1999. He received the B.Eng. degree in 2022 from the Wuhan University of Technology, Wuhan, China, where he is currently working toward the M.A.Eng. degree with the School of Mechanical and Electronic Engineering.

His main research interests include wireless transmission technology based on magnetic resonance.

Ian Robertson (Fellow, IEEE) received the B.Sc. (Eng.) and Ph.D. degrees in electronic and electrical engineering from King's College, University of London, Londodn, U.K., in 1984 and 1990, respectively.

Since 2004, he has been Professor with the School of Electronic and Electrical Engineering, University of Leeds, Leeds, U.K. He was the Director of learning and teaching from 2006 to 2011, the Head of school from 2011 to 2016, and the Programme Manager for the online M.Sc. in engineering management from 2017 to 2022. He was with the University of Surrey, Guildford, U.K., and King's College London, London. He has authored or coauthored more than 500 peer-reviewed research papers, edited the book MMIC DESIGN (IEE, 1995), and coedited *RFIC & MMIC Design and Technology* (published in English in 2001, and in Chinese in 2007) and *Microwave and Millimetre-Wave Design for Wireless Communications* (Wiley, 2016). His research interests include RF and microwave engineering.

Dr. Robertson was elected Fellow of the IEEE in 2012 in recognition of his contributions to MMIC design techniques and millimetre-wave system-in-package technology. He was the General Technical Programme Committee Chair for the European Microwave Week in 2011 and 2016.